

Article

Constructing Robust Solid Electrolyte Interface via ZrO₂ Coating Layer for Hard Carbon Anode in Sodium-Ion Batteries

Yuteng Gong¹, Chengxin Yu¹, Yu Li^{1,*}, Ji Qian¹, Chuan Wu^{1,2} and Ying Bai^{1,*}¹ School of Materials Science and Engineering, Beijing Institute of Technology, Beijing 100081, China² Yangtze Delta Region Academy of Beijing Institute of Technology, Jiaxing 314019, China

* Correspondence: liyu0820@bit.edu.cn (Y.L.); membrane@bit.edu.cn (Y.B.)

Abstract: Hard carbon (HC) has attracted extensive attention due to its rich material source, environmental non-toxicity, superior sodium storage capacity, and lower sodium storage potential, and is considered most likely to be a commercial anode material for sodium-ion batteries (SIBs). Nevertheless, the limited initial Coulombic efficiency (ICE) of HC is the main bottleneck hindering its practical application. To alleviate this issue, herein, a ZrO₂ coating was skillfully constructed by using a facile liquid phase coating method. The ZrO₂ coating can act as a physical barrier to prevent direct contact between the HC surface and the electrolyte, thus effectively reducing irreversible sodium adsorption and inhibiting the continuous decomposition of the electrolyte. Meanwhile, this fresh interface can contribute to the generation of a thinner solid electrolyte interface (SEI) with high ionic conductivity. As a result, the ICE of the ZrO₂-coated HC electrode can be optimized up to 79.2% (64.4% for pristine HC). Furthermore, the ZrO₂-coated HC electrode delivers outstanding cyclic stability so that the capacity retention rate can reach 82.6% after 2000 cycles at 1 A g⁻¹ (55.8% for pristine HC). This work provides a flexible and versatile surface modification method to improve the electrochemical property of HC, and hopefully accelerate the practical application of HC anodes for SIBs.



Citation: Gong, Y.; Yu, C.; Li, Y.; Qian, J.; Wu, C.; Bai, Y. Constructing Robust Solid Electrolyte Interface via ZrO₂ Coating Layer for Hard Carbon Anode in Sodium-Ion Batteries. *Batteries* **2022**, *8*, 115. <https://doi.org/10.3390/batteries8090115>

Academic Editor: Pascal Venet

Received: 15 July 2022

Accepted: 2 September 2022

Published: 6 September 2022

Publisher's Note: MDPI stays neutral with regard to jurisdictional claims in published maps and institutional affiliations.



Copyright: © 2022 by the authors. Licensee MDPI, Basel, Switzerland. This article is an open access article distributed under the terms and conditions of the Creative Commons Attribution (CC BY) license (<https://creativecommons.org/licenses/by/4.0/>).

Keywords: sodium-ion battery; hard carbon anode; ZrO₂ coating; solid electrolyte interface

1. Introduction

Developing green and low-carbon renewable resources is an important strategy to achieve sustainable development. Increasing attention has been paid to the exploitation and utilization of clean renewable energy, such as solar energy, water energy, and wind energy. However, the output of these renewable resources is intermittent and particularly vulnerable to the effects of time, space, and seasonal climate changes, which can severely limit the stable operation of the electrical grids. To date, constructing various large-scale energy storage systems is an effective tactic to ameliorate this issue. Electrochemical energy storage, which mainly includes secondary battery technology, has attracted extensive attention due to its superiorities of flexibility and convenience, easy maintenance, high energy density, and reliable conversion efficiency [1]. Therefore, lithium-ion batteries (LIBs) have been widely applied to various portable electronic devices since their commercialization [2]. Especially in recent years, with the rapid development of the electric vehicle industry, the demand for LIBs has increased sharply. Nevertheless, the limited abundance in the earth's crust and uneven geographical distribution of lithium resources result in the increasing cost of LIBs year by year, hindering their further application in the field of energy storage [3]. In contrast, sodium-ion batteries (SIBs) have inexhaustible sodium resources and low cost, and their electrochemical reaction mechanisms are similar to those of LIBs [4,5]. Based on this, developing SIBs as an imperative alternative to LIBs has a positive significance for large-scale energy storage systems [6–10].

The high-performance anode materials are essential for the large-scale commercialization of SIBs. Although the graphite anode has been successfully commercialized in LIBs, its

sodium storage performance in SIBs is poor, mainly due to the larger radius of Na^+ and the instability of the sodium-graphite intercalation compounds [11]. Therefore, most studies on anode materials for SIBs has turned to non-graphite carbon. Hard carbon (HC) has a higher Na storage capacity ($>300 \text{ mAh g}^{-1}$) and lower Na storage potential ($<0.1 \text{ V}$), and it is considered to be one of the most promising anode materials for SIBs [12–14]. HC can be obtained by processing resource-rich biomass materials (sucrose [11], coconut shell [15], shaddock peel [16], etc.) and natural polymers (polyvinylpyrrolidone [17], polyvinyl chloride [18], polyaniline [19], etc.). According to an associated report, the HC anode can provide a sodium storage capacity comparable to the lithium storage capacity provided by the graphite anode [12]. However, there are still some problems in such anode materials [13]. The most prominent one is that HC materials show low initial Coulombic efficiency (ICE), meaning that large amounts of sodium ions are irreversibly consumed in the first cycle, which seriously diminish the energy density and cycling stability of the batteries [13]. The limited ICE is mainly caused by two reasons. One is that the hard carbon material itself has a mass of defects and functional groups that can serve as active sites to irreversibly capture sodium ions. The other is that hard carbon materials have a high specific surface area, which can induce the continuous reaction of the electrolyte and the formation of disordered solid electrolyte interface (SEI) film, as well as some undesired side reactions [13,20]. To mitigate these issues, some well-thought-out strategies have been proposed, such as surface engineering, structural design and composition regulation, and so on [13].

In surface engineering, surface coating technology is generally regarded as a serviceable method to ameliorate the ICE of hard carbon materials [21–23]. The new versatile interface is committed to suppressing the decomposition of electrolytes by avoiding direct contact between the hard carbon surface and electrolytes, thus reducing adverse side reactions and promoting the formation of well-functioning SEI films. Carbon is often used as a remarkable coating material for the hard carbon anodes of SIBs by virtue of its excellent electrochemical stability and general applicability to common electrolyte systems [13]. For example, Hu's group [24] successfully synthesized hard carbon with a soft carbon coating by pyrolyzing toluene, and the as-prepared material exhibits a relatively high ICE of 83%, while for the uncoated material, only 53%. Ponrouch et al. [25] used a simple physical method to coat a carbon layer on the HC surface, which significantly improved the ICE from 55% to 70%. Recently, He et al. [26] also increased the ICE to 94.1% by adding a soft carbon coating to the hard carbon surface. In addition, oxide coating has also been widely studied and applied in the field of new energy storage materials. Therefore, Al_2O_3 coating has been tipped to be available in both SIBs and LIBs to optimize electrochemical performance. Using atomic layer deposition (ALD), Lu et al. [27] elaborately devised an Al_2O_3 artificial SEI-coated hard carbon anode of an SIB. The deposited Al_2O_3 film not only makes the electrode exhibit high capacity and superior cycling stability, but also improves the ICE from 67% to 75%. Lin [28] also proved that ultrafine Al_2O_3 nanoclusters can cover the defects on the surface of carbon materials and effectively lessen the decomposition of electrolytes, thus promoting the generation of a thin and homogenous SEI. Recently, our group constructed an amorphous Al_2O_3 layer on a HC surface using an easy-operation coating method [23], which remarkably improved the ICE of HC from 64.7% to 81.1%. The Al_2O_3 coating can reduce irreversible capacity loss by regulating the microscopic disorder of the HC surface. Furthermore, the homotype heterojunctions formed by HC and coating can induce the formation of an SEI with a regular distribution of organic and inorganic components. In the field of LIBs, Al_2O_3 coating is also considered to be capable of effectively reducing the irreversible consumption of electrode materials and the regeneration of SEI films [29]. Besides, ZrO_2 coating also makes a considerable contribution to the almost unassailable position of LIBs. The electrochemical properties of a myriad of electrode materials, such as $\text{LiNi}_{0.8}\text{Co}_{0.1}\text{Mn}_{0.1}\text{O}_2$ [30], Li_xCoO_2 [31], $\text{LiNi}_{0.6}\text{Co}_{0.2}\text{Mn}_{0.2}\text{O}_2$ [32], $\text{Li}[\text{Ni},\text{Mn},\text{Co}]\text{O}_2$ [33], $\text{LiNi}_{1/3}\text{Co}_{1/3}\text{Mn}_{1/3}\text{O}_2$ [34], $\text{Li}[\text{Ni}_{0.5}\text{Mn}_{0.3}\text{Co}_{0.2}]\text{O}_2$ [35], and so on, have been improved in varying degrees with the optimization of a ZrO_2 coating. However, the research on ZrO_2

coating for SIBs is still in the blank stage, and there is no elaborate report about it at present. Therefore, it is with great foresight that we explore an appropriate method to construct a versatile ZrO_2 coating on the hard carbon anode surface of SIBs, which can be expected to reduce irreversible sodium ion adsorption and optimize the interface properties, in turn improving the ICE and cycling stability of electrode materials.

Herein, inspired by the extensive application of ZrO_2 coating in LIBs, we coated the HC surface with a ZrO_2 coating to prepare the HC@ZrO_2 material, by using a facile liquid phase coating method. Unlike chemical or physical vapor deposition (CVD, PVD) and atomic layer deposition (ALD), which is commonly used in previous research requiring sophisticated equipment and unmanageable operation processes, the method we adopted only requires two simplified and feasible processes: aqueous phase coating and calcination. The well-designed ZrO_2 coating can act as a physical barrier to prevent more active sites from being exposed to the electrolyte, thus reducing the uncontrolled decomposition of the electrolyte. At the same time, the ZrO_2 coating can effectively inhibit the continuous destruction and regeneration of SEI, forming thinner SEI with lower electrochemical impedance, which facilitates the electrochemical reaction kinetics. The electrochemical performances of the as-prepared HC@ZrO_2 electrodes are significantly enhanced with ICE as high as 79.2%, with excellent cycling performance. The capacity can maintain 82.6% under 1 A g^{-1} after 2000 cycles. In striking contrast, the ICE of pristine HC without coating is only 64.4%, and the cycling stability is inferior (a capacity retention of 55.8% under 1 A g^{-1} after 2000 cycles). This study has a certain enlightening effect and it can open up a new way to accelerate the commercial application of SIBs.

2. Experimental Section

2.1. Synthesis and Characterization of HC and HC@ZrO_2

HC was prepared by a facile hydrothermal process followed by the carbonization of sucrose (Aladdin, Shanghai, China). First, 6 g sucrose was completely dissolved in 70 mL deionized water (DW). Then, the above solution was transferred to a 100 mL Teflon-lined stainless steel autoclave and heated at $170 \text{ }^\circ\text{C}$ for 10 h. The precipitation was centrifuged and washed with DW and ethanol, and dried in an oven at $100 \text{ }^\circ\text{C}$ overnight. Finally, the obtained material was calcinated at $1200 \text{ }^\circ\text{C}$ for 2 h with a heating rate of $5 \text{ }^\circ\text{C min}^{-1}$ under Ar atmosphere. The as-prepared powder was pristine HC.

The HC@ZrO_2 materials were prepared using a liquid phase coating method. First, 2 mg $\text{C}_{12}\text{H}_{28}\text{O}_4\text{Zr}$ (Meryer, Shanghai, China) was completely dissolved in 20 mL ethanol, and then 200 mg HC was added into the mixture. Second, while stirring vigorously, the obtained suspension was heated in a water bath to $60 \text{ }^\circ\text{C}$ until the mixture was completely dry. Third, the solids were vacuum-dried at $110 \text{ }^\circ\text{C}$ for 12 h. Finally, the dried solids were transferred to a tubular furnace and heated at $600 \text{ }^\circ\text{C}$ for 5 h; HC@ZrO_2 -1 was synthesized. Keeping the same reaction conditions, except for changing the mass of $\text{C}_{12}\text{H}_{28}\text{O}_4\text{Zr}$, HC@ZrO_2 -0.5, HC@ZrO_2 -1.5, HC@ZrO_2 -3, and HC@ZrO_2 -1 were synthesized.

The morphologies and microstructure of the HC and HC@ZrO_2 samples were characterized with scanning electron microscopy (SEM, Carl Zeiss AG, Zeiss Supra 55, Oberkochen, Germany) and a transmission electron microscope (TEM, JEOL, JEM-ARM200CF, Tokyo, Japan). Energy dispersive X-ray spectroscopy was performed to observe the element distribution. The X-ray diffraction (XRD, Rigaku, MiniFlex 600, Tokyo, Japan) was used to analyze the crystalline structure of HC and HC@ZrO_2 . X-ray photoelectron spectroscopy (XPS, ULVAC-PHI, PHI QUANTERA-II SXM, Chigasaki, Japan) was recorded to examine the element composition and surface state of HC and HC@ZrO_2 . The specific surface area and pore size information were obtained using the Brunauer–Emmett–Teller (BET) equation on N_2 adsorption-desorption isotherms measured by a BELSORP-max II instrument (MicrotracBEL Japan, Inc. MicrotracBEL, BELSORP-max II, Osaka, Japan) at 77.4 K .

2.2. Electrochemical Measurements

The working electrodes were prepared by mixing 80 wt% active material, 10 wt% super P, and 10 wt% polymer binders (polyvinylidene (PVDF)). The slurry was coated onto copper foil followed by vacuum drying at 90 °C for 24 h. The 2025-type coin cells were assembled in an Ar-filled glove box (MBRAUN, LabStar, Shanghai, China, $O_2 < 0.1 \times 10^{-6}$, $H_2O < 0.1 \times 10^{-6}$) using a Na metal counter electrode. The electrolyte was 1 mol L⁻¹ NaPF₆ dissolved in ethylene and diethyl carbonate (EC:DEC, 1:1 in volume). The charge-discharge tests were performed on a LAND CT2001A instrument at selected current densities. Cyclic voltammetry (CV) and electrochemical impedance spectroscopy (EIS) tests were all carried out on an electrochemical workstation (CHI660E). The CV tests were performed in the voltage range from 0.01 to 2.80 V at a scan rate of 0.1 mV s⁻¹, and the EIS tests were performed with an amplitude of 10 mV and frequency of 1×10^5 – 1×10^{-2} Hz.

3. Results and Discussion

The ZrO₂ coating was constructed as a physical barrier of HC to reduce the occurrence of irreversible side reactions and excessive decomposition of the electrolyte, thus improving the ICE. The raw HC was obtained by a facile hydrothermal process followed by the carbonization of sucrose. Then, the obtained HC material was modified as HC@ZrO₂ according to the experimental steps described in Figure S1 in the supplementary materials. To obtain the best-performing material, various HC@ZrO₂ materials with ZrO₂ and HC mass ratios of 0.5%, 1%, 1.5%, 3%, and 5% were synthesized, and each sample was named HC@ZrO₂-0.5, HC@ZrO₂-1, HC@ZrO₂-1.5, HC@ZrO₂-3, and HC@ZrO₂-5, respectively. Figure 1 and Supplementary Figure S2 exhibit the morphological characterizations of HC and HC@ZrO₂. As shown in the scanning electron microscope (SEM) (Figures 1a and S2a) images, the uncoated hard carbon materials appear spherical or gourd shaped with a smooth surface and an average diameter of about 800 nm, which is consistent with the previous reports [24]. It can be clearly observed from Figure 1b–f that there is no significant change in the shape and size of HC after ZrO₂ coating, and only a light-colored and evenly distributed villiform coating appears on the surface, indicating an ultrathin ZrO₂ coating layer. With the increase of the ZrO₂ ratio, the surface coating was made thicker and thicker. Therefore, HC@ZrO₂-0.5 is covered with less ZrO₂ and even some smooth HC is exposed, while the material surface of HC@ZrO₂-5 is covered with a dense villiform coating layer, suggesting that this ZrO₂ coating is the thickest among all the samples, which can be more intuitively observed from Figure S2b–f. To further figure out the composition of the HC surface coating, energy dispersive X-ray spectroscopy (EDX) was used in conjunction with SEM. According to scanning results of mapping (Figure 1g), it is easy to observe that elements C, O, and Zr are evenly distributed on the HC surface, meaning that the ZrO₂ coating was successfully constructed.

The transmission electron microscopy (TEM) images were adopted to further observe the microstructure of HC and HC@ZrO₂-1. As shown in Figure S3a and Figure 1h, the surface of the original HC is very smooth, and after further magnification (Figure S3b), it can clearly be seen that the sucrose-derived HC possesses a highly disordered structure. In contrast, TEM images of the modified HC@ZrO₂-1 material show an obvious difference from HC (Figures S3c and 1i,j). A distinctive coating appears on the surface of the HC@ZrO₂-1 material, which is evenly distributed on the HC surface, making its surface become rougher. The functionalized coating plays a crucial part in protecting defects and reducing irreversible capacity. Based on the results of selected area electron diffraction (SAED) in Figure 1k, it can be concluded that the ZrO₂ coating's own partial crystal structure, unlike the highly disordered structure of HC, can fill and shield the defects and active sites on the HC surface. In addition, a TEM-DES line scan of HC@ZrO₂-1 (Figure 1l) shows that Zr content is highest at the edge of the carbon sphere and the subsequent distribution is uniform, indicating the uniform distribution of Zr on the HC surface, which echoes the EDS results. In brief, depending on the SEM and TEM, it is presumed that the ZrO₂ coating

exists on the surface of the HC@ZrO₂ material and the thickness of the coating can be changed by controlling the value of the ZrO₂ content.

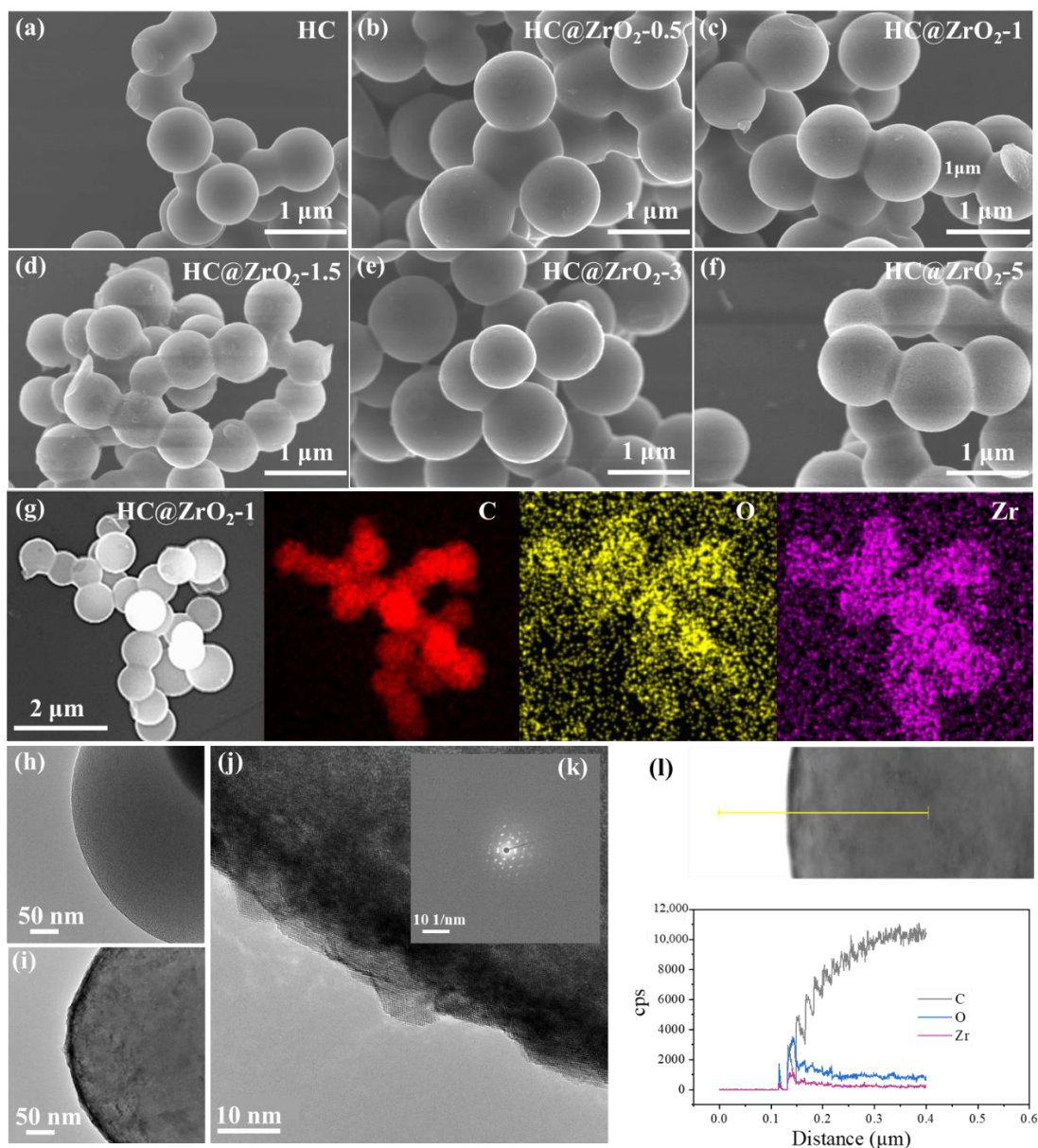


Figure 1. SEM images of HC (a) and HC@ZrO₂ (b–f) with different ZrO₂ content. (g) EDS elemental maps of HC@ZrO₂-1. TEM images of HC (h) and HC@ZrO₂-1 (i,j). (k) SAED image of HC@ZrO₂-1. (l) TEM-DES line scan of HC@ZrO₂-1.

To further confirm the presence of ZrO₂, the HC and HC@ZrO₂ materials were characterized by X-ray diffraction (XRD). As depicted in Figure 2a, pristine HC has two wide diffraction peaks of 22.3° and 43.6° at around 2θ , and the peaks are assigned to (002) and (101) planes, respectively, demonstrating that HC has an amorphous structure [22]. Moreover, the values of $d_{(002)}$ and $d_{(101)}$ can be calculated as 3.98 Å and 2.07 Å, respectively, by the Bragg equation. As for the XRD patterns of HC@ZrO₂, the wide peaks at $2\theta = 22.3^\circ$ and 43.6° still exist, indicating that the construction of the ZrO₂ coating has no effect on the original HC crystal structure. However, with the increase of the ZrO₂ proportion, some distinct diffraction peaks appear at around $2\theta = 30.1^\circ, 34.9^\circ, 50.2^\circ, 59.7^\circ, 62.7^\circ,$ and 73.9° , which can all be indexed from the standard pattern of ZrO₂ (JCPDS 49-1642). The layer spacing and corresponding crystal information are shown in Supplementary Table S1. Combined

with XRD and TEM analysis, it is confirmed that the liquid phase coating method can successfully coat the crystal-structured ZrO_2 on an HC surface without changing the intrinsic structure of HC. X-ray photoelectron spectroscopy (XPS) was used to further investigate the effect of the ZrO_2 coating on the HC surface, and Figure 2b shows the full spectra of HC, $\text{HC@ZrO}_2\text{-1}$, and $\text{HC@ZrO}_2\text{-5}$. It is observed that unmodified HC has three obvious peaks, which belong to C 1s, O 1s and O KLL, respectively. With the ZrO_2 coating, C 1s, O 1s, and O KLL peaks still exist, and with the increase of the ZrO_2 ratio, the peak intensity of C 1s decreases, while the O 1s and O KLL peak intensities increase. In addition, the XPS spectra of $\text{HC@ZrO}_2\text{-1}$ and $\text{HC@ZrO}_2\text{-5}$ show Zr-related peaks corresponding to Zr 3s, Zr 3d, and Zr 3p, respectively [36]. The peak intensity of $\text{HC@ZrO}_2\text{-5}$ is higher than that of $\text{HC@ZrO}_2\text{-1}$, suggesting that $\text{HC@ZrO}_2\text{-5}$ contains the most ZrO_2 , which is consistent with SEM and TEM analyses. To explore the effect of the ZrO_2 coating on the HC specific surface area, the Brunauer–Emmett–Teller (BET) specific surface area test was performed on the HC and $\text{HC@ZrO}_2\text{-1}$ materials, and the results are summarized in Table S2. According to the density functional theory (DFT) pore size distribution in Figure 2c, it can be known that HC has abundant micropores with an average pore volume of $0.014 \text{ cm}^3 \text{ g}^{-1}$ and an average pore size of 1.48 nm. Although the $\text{HC@ZrO}_2\text{-1}$ material is also dominated by micropores, the pore volume and pore size are larger, with an average pore volume of $0.022 \text{ cm}^3 \text{ g}^{-1}$ and an average pore size of 3.87 nm. In addition, the results of the N_2 adsorption-desorption test (Figure 2d) reveal that the specific surface area of HC is $17.84 \text{ m}^2 \text{ g}^{-1}$, while the specific surface area of the modified $\text{HC@ZrO}_2\text{-1}$ material increases to $22.35 \text{ m}^2 \text{ g}^{-1}$. The increase in specific surface area, pore volume, and pore size may be due to the large specific surface area of the ZrO_2 coating itself, although the irregularly shaped ZrO_2 can fill and shield the inherent defects and active sites of HC.

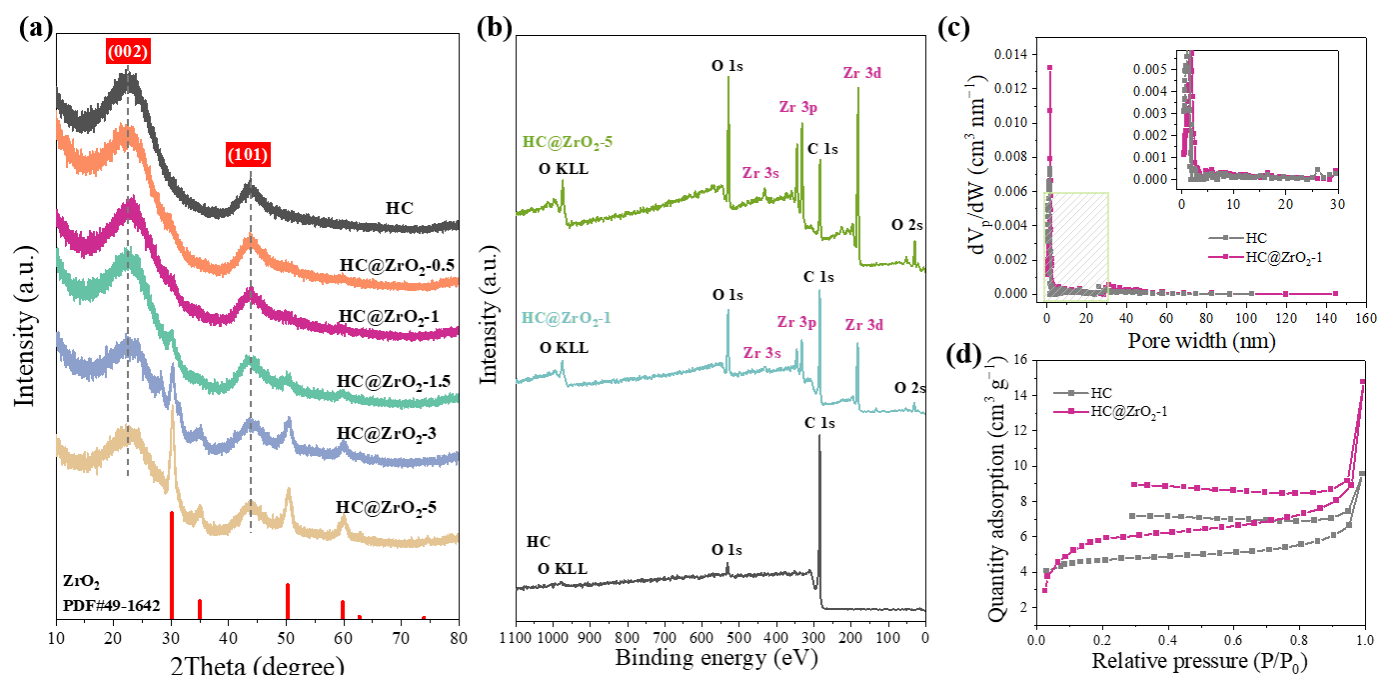


Figure 2. (a) XRD patterns of HC and HC@ZrO_2 . (b) XPS of HC, $\text{HC@ZrO}_2\text{-1}$, and $\text{HC@ZrO}_2\text{-5}$. (c) The density functional theory (DFT) pore size distribution of HC and $\text{HC@ZrO}_2\text{-1}$. (d) N_2 adsorption-desorption measurements of HC and $\text{HC@ZrO}_2\text{-1}$.

To provide insight into the effect of the ZrO_2 coating on the electrochemical properties, HC and HC@ZrO_2 were used as working electrodes to assemble half cells for galvanostatic charge and discharge. As can be seen from the initial charge-discharge curves at a current density of 50 mA g^{-1} shown in Figure 3a, the curves of HC@ZrO_2 and HC are basically the same in shape, with a sloped area and a platform area, which correspond to the typical electrochemical characteristics of HC in SIBs [11,37]. Simultaneously, this also proves

that the ZrO_2 coating does not change the HC structure and sodium storage mechanism. Slightly different from the charge-discharge curve of HC, the ZrO_2 coating significantly reduced the irreversible voltage transition of HC, which is about 1.0 V, corresponding to the process of SEI formation and electrolyte decomposition [38], representing that the electrolytic decomposition and SEI formation of HC and HC@ZrO_2 materials are different. The ZrO_2 coating can significantly inhibit the electrolyte decomposition reaction at ~ 1.0 V, thus cutting down the irreversible capacity in the initial charge-discharge process. The corresponding initial reversible capacities and ICE of the HC and HC@ZrO_2 materials are shown in Table S3. It was noticed that the ICE of HC@ZrO_2 is higher than that of unmodified HC (ICE is 64.4%). Specifically, the ICE values of $\text{HC@ZrO}_2\text{-0.5}$, $\text{HC@ZrO}_2\text{-1}$, $\text{HC@ZrO}_2\text{-1.5}$, $\text{HC@ZrO}_2\text{-3}$, and $\text{HC@ZrO}_2\text{-1}$ are 77.3%, 79.2%, 75.2%, 72.8%, and 71.8%, respectively. Figure S4 shows the cyclic voltammetry (CV) tests of HC and $\text{HC@ZrO}_2\text{-1}$. As can be seen from the profiles, all curves show a pair of reversible redox peaks at around 0.1 V, suggesting that the ZrO_2 coating does not change the internal structure of HC. In addition, HC shows an irreversible broad cathodic peak between 0.3 and 1.0 V, which is relative to the decomposition of the electrolyte and the formation of SEI. Surprisingly, the intensity of the corresponding peak in the $\text{HC@ZrO}_2\text{-1}$ curve is greatly reduced, suggesting that the ZrO_2 coating can effectively reduce the irreversible capacity by suppressing the electrolyte decomposition. To have an in-depth understanding of the influence of the ZrO_2 coating on electrolyte decomposition, differential capacity analysis was carried out on HC and $\text{HC@ZrO}_2\text{-1}$, and the results are shown in Figure 3b. The plots of both pristine HC and HC@ZrO_2 show a pair of reversible redox peaks at around 0.1 V, which correspond to the intercalation behavior of Na^+ in HC [27,39,40]. Furthermore, as can be seen from the insert of Figure 3b, the peak intensities at ~ 0.53 V, ~ 0.71 V, and ~ 1.12 V decrease significantly after ZrO_2 coating, which further confirms that the ZrO_2 coating can effectively suppress the decomposition of the electrolyte and contribute to the in situ generation of a thin SEI at the HC–electrolyte interface, which is the reason why the HC@ZrO_2 materials can enhance ICE. Figure 3c details the correlation between the ZrO_2 coating proportion and some specific electrochemical properties of the electrodes. For comparison, $\text{HC@ZrO}_2\text{-1}$ exhibits the highest ICE (79.2%), which is 14.8% higher than unmodified HC (64.4%). From the holistic perspective, with the increase of the ZrO_2 coating proportion, ICE increases first and then decreases, while the slope capacity decreases, and the platform capacity stays constant first and then decreases. With lower ZrO_2 content ($<1\%$), ICE increases gradually, slope capacity decreases, and platform capacity remains unchanged, which can be attributed to the fact that the ZrO_2 coating effectively prevents direct contact between the electrolyte and HC surface active sites, significantly hindering the irreversible decomposition of the electrolyte [13,41,42]. However, when the content of ZrO_2 continues to increase, all three indicators show a downward trend, which may be because too much ZrO_2 leads to a too-thick coating that sodium ions cannot enter smoothly. The ZrO_2 coating can effectively reduce sodium storage sites on the surface of HC that derived from defects and functional groups, and has no effect on sodium ion insertion behavior. Therefore, the continuous decrease in slope capacity can verify that sodium ions correspond to the “adsorption” mechanism in the HC slope region, while the lack of an obvious decrease in platform capacity indicates that sodium ions are subject to the “insertion” mechanism in the platform region [43,44].

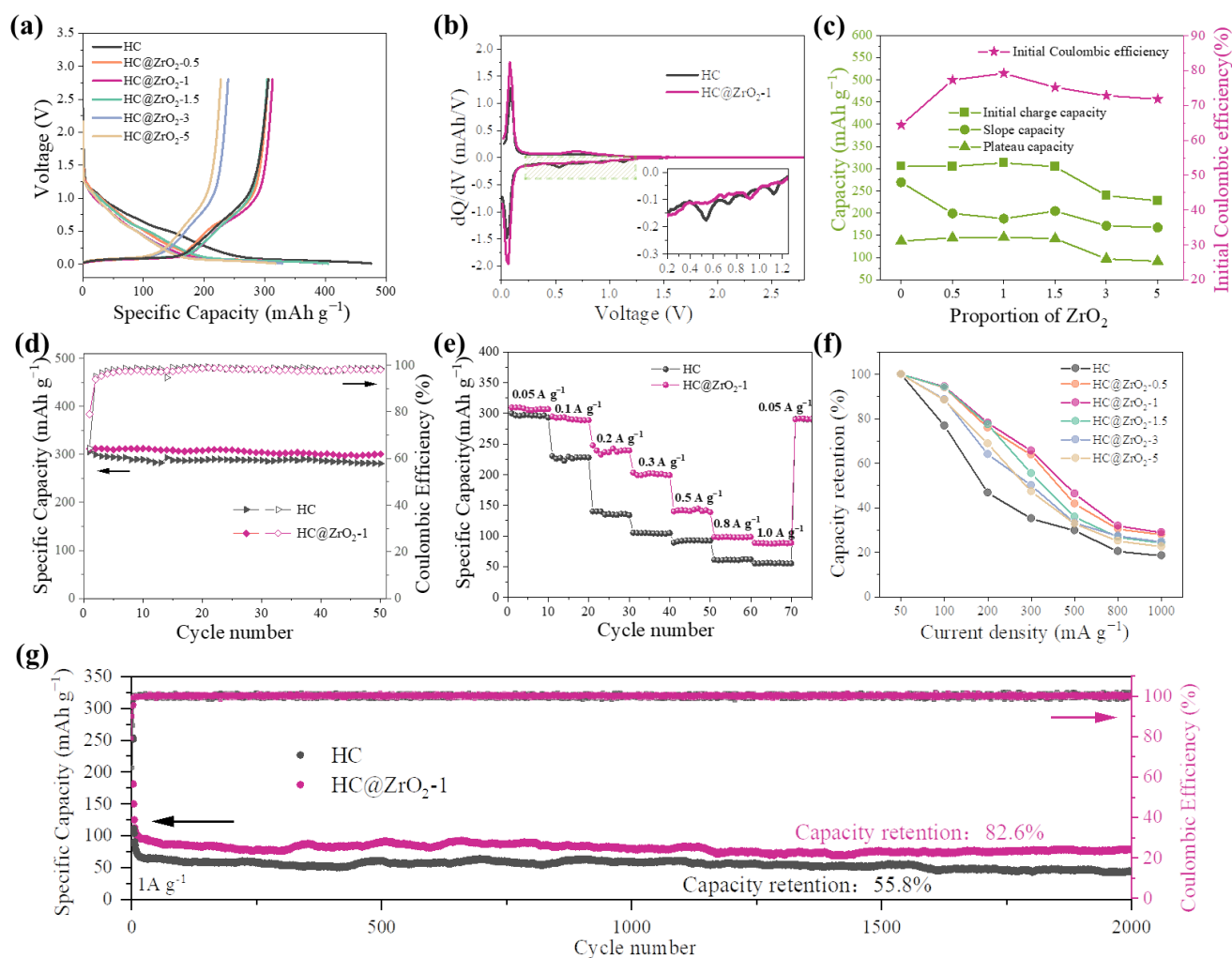


Figure 3. (a) Initial galvanostatic charge-discharge profiles of the HC and HC@ZrO₂ electrodes at 50 mA g⁻¹. (b) The dQ/dV versus voltage plots for the HC and HC@ZrO₂-1 electrodes. (c) Summary of ICE, charge capacity, slope capacity, and plateau capacity of the HC and HC@ZrO₂ electrodes. (d) Cycling performance of the HC and HC@ZrO₂-1 electrodes at 50 mA g⁻¹. (e,f) Rate performance and corresponding line chart of the HC and HC@ZrO₂ electrodes. (g) Long cycling performance of the HC and HC@ZrO₂-1 electrodes at 1 A g⁻¹.

To fully ascertain the effect of the ZrO₂ coating on electrochemical performance, we further compared the cyclic stability and rate performance of HC and HC@ZrO₂. Figures 3d and S5a show the cyclic performance test at a current density of 50 mA g⁻¹. After 50 cycles, HC@ZrO₂-1 exhibits the best reversible capacity of 300.8 mA h g⁻¹ with an extremely high capacity retention rate. However, the capacities of HC@ZrO₂-3 (200.9 mA h g⁻¹) and HC@ZrO₂-5 (195.6 mA h g⁻¹) are both lower than that of HC (Figure S5a), which may be attributed to the fact that too much ZrO₂ hinders the sodium ions intercalation, thus reducing the platform capacities. Accordingly, Figure S5b shows the charge-discharge profiles for the selected cycles of HC and HC@ZrO₂-1. HC@ZrO₂-1 has lesser slope capacity, which indicates that the ZrO₂ coating can effectively reduce HC surface defects, thus reducing the irreversible sodium storage capacity. Simultaneously, the Coulombic efficiency of HC@ZrO₂-1 increases rapidly to 95.3% after the first cycle (79.2%), then remain stable at about 98% during the subsequent cycles, indicating that HC@ZrO₂-1 is capable of keeping a relatively complete structure during the long-term cycle. Figures 3e,f and S5c show the rate properties of the HC and HC@ZrO₂ materials. Among them, HC@ZrO₂-1 shows the most outstanding rate performance, with a reversible capacity of 307.2 mA h g⁻¹ at 0.05 A g⁻¹.

Even at the relatively high current density of 1.0 A g^{-1} , it is still able to deliver a reversible capacity of 88.6 mAh g^{-1} , while unmodified HC only has a capacity of 58.4 mAh g^{-1} , with a larger capacity fade (capacity retention rate is 18.4%). Subsequently, the galvanostatic charge and discharge of HC and HC@ZrO₂-1 at a high current density of 1 A g^{-1} was performed to further figure out the optimization effect of ZrO₂ coating. It can be observed from Figure 3g that after 2000 cycles, the HC@ZrO₂-1 material exhibits no obvious capacity fade with an outstanding capacity retention rate of 82.6%, which is far superior to pristine HC (the capacity retention rate is only 55.8%). The superior rate performance and cycle stability of HC@ZrO₂ can be attributed to the reasonable modification of the HC surface by the ZrO₂ coating. Based on the above various electrochemical data, it can be concluded that constructing an appropriate amount of ZrO₂ coating (the mass ratio of HC is 1%) on a hard carbon surface can prevent surface defects from irreversibly capturing sodium ions, and can inhibit the occurrence of some unprofitable side reactions. Additionally, as shown in Table S4, compared to the published reports, the improvement of the ICE of the ZrO₂ coating on HC is more outstanding, and the preparation method is relatively facile.

To investigate the specific improvement of the ZrO₂ coating on the SEI, SEM examinations of the cycled HC and HC@ZrO₂-1 materials were utilized. As can be seen from Figure 4a–c, the originally smooth HC surface becomes very rough in the full discharge state (0.01 V), indicating that a large number of SEI layers are generated. In particular, it can be seen more clearly that many thick and uneven SEI layers appear at the intersection of the two carbon spheres (Figure 4c). The inferior SEI probably derives from the uncontrollable decomposition of the electrolyte and the occurrence of some uncertain side reactions. In sharp contrast, the surface of HC with a uniform ZrO₂ coating can remain in a relatively smooth state after cycling (Figure 4d,e). Even where two carbon spheres meet, there is no noticeable SEI layer accumulation (Figure 4f), meaning that the ZrO₂ coating can promote the formation of a thinner SEI. Electrochemical impedance spectroscopy (EIS) was performed to investigate the charge transfer kinetics and SEI evolution of HC and HC@ZrO₂ in more detail. Figure 4g shows the EIS results of HC || Na and HC@ZrO₂ || Na half cells in an initial open circuit voltage state. With the increase of ZrO₂ content, the electrode impedance increases gradually, which may be caused by the poor conductivity of ZrO₂ [30]. A too-thick ZrO₂ layer can hinder the diffusion of sodium ions, which corresponds to the above conclusion that the platform capacity and specific capacity decrease due to too much ZrO₂. To avoid interference of counter electrodes, the interface properties of HC and HC@ZrO₂-1 were further studied by using a three-electrode setup, as shown in Figure S6a. As can be observed from the EIS results of HC and HC@ZrO₂-1 discharged to 0.01 V, shown in Figure 4h, both curves have similar shapes, including two semicircles at a high frequency, which are related to the interfacial impedance (R_{SEI}) and charge transfer resistance (R_{CT}), as well as an upward-sloping line representing the Warburg impedance at a low frequency, which is related to Na⁺ diffusion in the electrode [45]. Compared to the initial EIS, the plots of cycled electrodes show an extra feature semicircle, which also confirms the generation of the SEI. The EIS curves are fitted according to the equivalent circuit shown in Figure S6b, and the results are summarized in Table S5. The R_{SEI} and R_{CT} of pristine HC are 113.3 Ω and 61.7 Ω , while those of HC@ZrO₂-1 are reduced to 79.2 Ω and 58.2 Ω , respectively. In addition, combined with Figure 4g,h, one can see that the impedance of cycled HC@ZrO₂-1 decreases significantly compared to that of the non-cycled anode. This is mainly because the ZrO₂-derived SEI is thin and uniform, with lower interfacial resistance and charge transfer resistance, which provides favorable conditions for the rapid migration of Na⁺. The EIS results of HC and HC@ZrO₂-1 samples after different cycles are shown in Figure S7. The R_{SEI} and R_{CT} of HC@ZrO₂-1 are always lower and change little after long cycles, while those of untreated HC are larger and increase with cycling, further indicating that the ZrO₂ coating can reduce the generation of the SEI, which is consistent with the results of SEM. Furthermore, the XPS was used to determine the effect of the ZrO₂ coating on the SEI components. Figure 4i shows the XPS full spectra of the HC and HC@ZrO₂-1 electrodes discharged to 0.01 V. The spectrum of HC@ZrO₂-1 not only contains characteristic peaks

of Na 1s, O KLL, F KLL, F 1s, O 1s, Na KLL, C 1s, and O 2s that can be observed in HC spectrum, but also shows the Zr 3d and 3p peaks, which also proves that ZrO₂ has been successfully coated on the HC surface [33]. Compared to the XPS spectra of non-cycled HC and HC@ZrO₂-1 shown in Figure 2b, the XPS spectra of the cycled anode in Figure 4i show distinct F 1s, Na 1s, and O 1s peaks, meaning that the electrolyte has decomposed and the SEI that has organic and inorganic components has formed. Yet, it is worth noting that the peak intensities of the Na 1s, F 1s, and O 1s characteristic peaks of HC@ZrO₂-1 which mainly derived from the decomposition of EC/DEC solvents and NaPF₆ salts, are lower than that of HC, further verifying the SEM conclusion that the ZrO₂ coating can effectively inhibit the decomposition of the electrolyte. The high-resolution Zr 3d, F 1s, and O 1s spectra were fitted to obtain a more definite conclusion about the difference between the HC and HC@ZrO₂-1 SEI, as shown in Figure 4j-l. According to the Zr 3d spectrum of HC@ZrO₂-1 in Figure 4j, the characteristic peaks for Zr 3d_{3/2} and Zr 3d_{5/2} are observed at 183.4 eV and 181.2 eV, respectively, representing the Zr⁴⁺ ions in ZrO₂ [32]. In addition, the peak at 184.0 eV is related to the Zr-F bond, suggesting that the ZrO₂ on the HC surface can react with electrolyte decomposition products and thus improve the stability of the SEI [28]. Both curves of F 1s show two peaks near 687 eV and 684.5 eV, which can be assigned to F-P and NaF, respectively, which are the main inorganic components of SEI [27]. Additionally, the F 1s spectrum of HC@ZrO₂-1 also shows a characteristic peak at 685.9 eV, which can be assigned to Zr-F, indicating the existence of the ZrO₂ coating [33]. Compared to HC, HC@ZrO₂-1 exhibits the weaker peak signal, suggesting that there are fewer inorganic components in the HC@ZrO₂-1 SEI. As we know, the NaF has poor ionic conductivity and excessive accumulation of NaF can severely hinder the diffusion of Na⁺, so the reduction of NaF is very beneficial, which is in accordance with the EIS results [46]. According to the O 1s spectra (Figure 4l), both plots can be divided into three characteristic peaks, namely ROCO₂Na (535.4 eV), C=O (532.5 eV), and C-O (531 eV), which mainly arose from the reduction of organic solvent in the electrolyte [46]. Except for these common peaks, the appearance of a Zr-O (530 eV) bond in the HC@ZrO₂-1 also proves the existence of the ZrO₂ coating. Similarly, the peaks in the HC@ZrO₂-1 show a lower intensity than HC. Therefore, combined with all of the above analyses, it can be concluded that ZrO₂ coating can successfully inhibit the reaction of electrolytes and promote the generation of a thinner SEI, in turn accelerating the electrochemical reaction kinetics and contributing to a better ICE, rate performance, and cycling performance of HC.

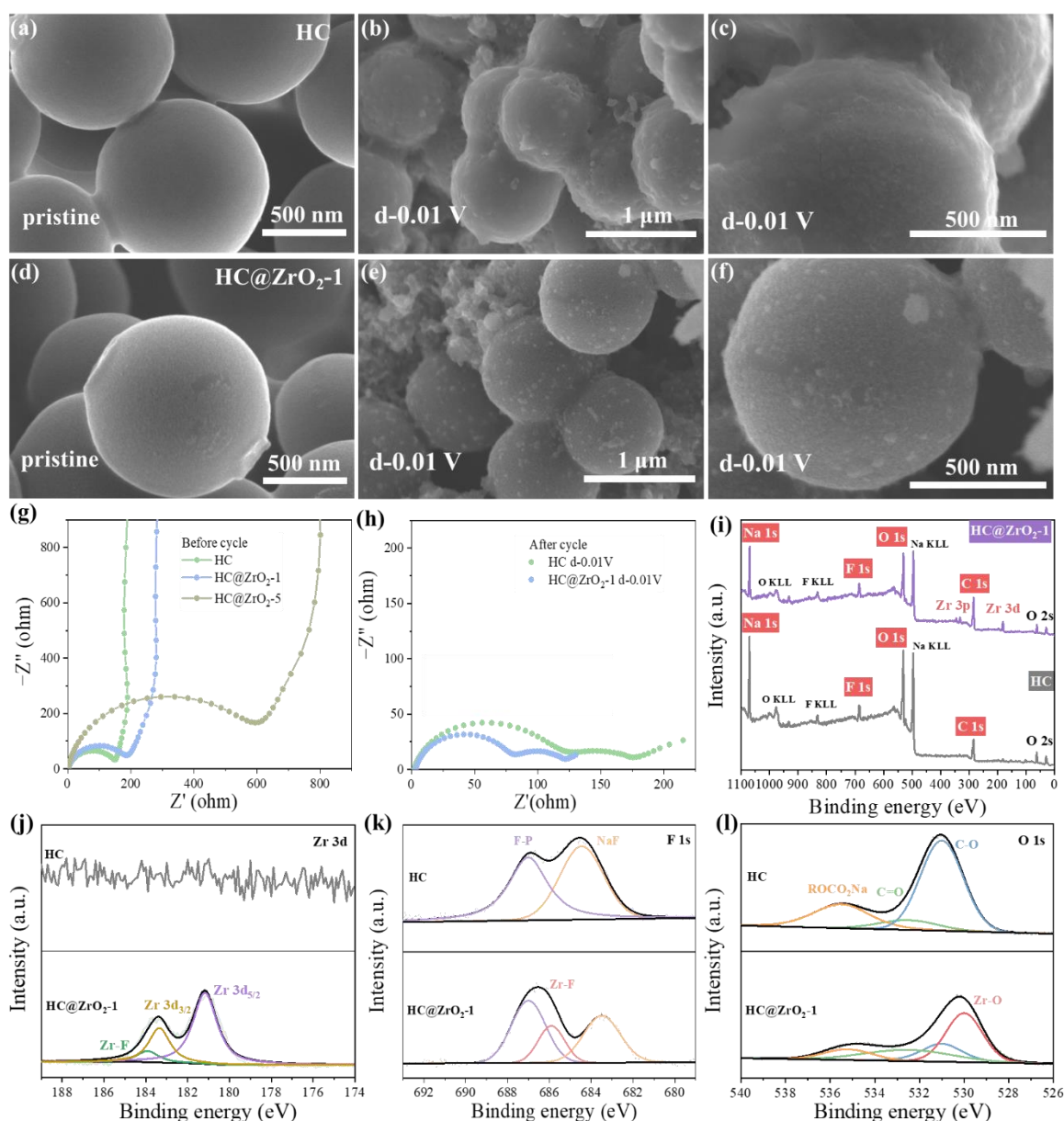


Figure 4. SEM images of HC (a–c) and HC@ZrO₂-1 (d–f) electrodes discharged to 0.01 V (d-0.01 V). (g) EIS plots of HC || Na and HC@ZrO₂ || Na half cells at initial open circuit voltage state; (h) EIS plots of HC and HC@ZrO₂-1 electrodes with the three-electrode setup at fully discharged state (d-0.01 V). XPS full spectra (i), the high-resolution Zr 3d (j), and the high-resolution F 1s (k) and O 1s (l) spectra of HC and HC@ZrO₂-1 electrodes discharged to 0.01 V.

4. Conclusions

In this paper, HC@ZrO₂ material was prepared by using a facile liquid coating method to coat the HC surface with an optimized ZrO₂ coating, which significantly improved the ICE and electrochemical properties of the HC anode. The ZrO₂ coating can act as a physical barrier to prevent the active sites on the hard carbon surface from contacting the electrolyte directly, thereby reducing irreversible sodium adsorption and excessive electrolyte decomposition. Furthermore, the ZrO₂ coating can facilitate the formation of a thinner and more stable SEI with a high ionic conductivity, which can diminish the interfacial resistance and accelerate the sodium storage kinetics. Consequently, the possession of the ZrO₂ coating can obviously improve the electrochemical properties without changing the internal structure and sodium storage mechanism of the pristine hard carbon. The HC@ZrO₂-1 material exhibits the enhanced ICE of 79.2% and outstanding

capacity of 313.2 mAh g⁻¹ at 50 mA g⁻¹. The cyclic stability is also significantly improved so that the capacity retention can achieve 82.6% after 2000 cycles at 1 A g⁻¹, while unmodified HC is only 55.8%. This study exhibits an efficient strategy for optimizing a HC anode, and provides a new path to realize the commercial application of high-performance SIBs.

Supplementary Materials: The following supporting information can be downloaded at: <https://www.mdpi.com/article/10.3390/batteries8090115/s1>, Figure S1: Schematic diagram of experimental process; Figure S2: SEM images of HC and HC@ZrO₂; Figure S3: TEM images of HC (a,b) and HC@ZrO₂-1 (c); Figure S4: The CV curves for the first two cycles for HC and HC@ZrO₂-1; Figure S5: (a) Cycling performance of the HC and HC@ZrO₂ electrodes at 50 mA g⁻¹. (b) Charge-discharge profiles of the HC and HC@ZrO₂-1 electrodes at different cycles. (c) Rate performance of the HC and HC@ZrO₂ electrodes. Figure S6: (a) Digital photo of three-electrode system. (b) The equivalent circuit of EIS curve; Figure S7: EIS plots of HC and HC@ZrO₂-1 electrodes after different cycles; Table S1: The layer spacing and corresponding crystal information of ZrO₂ (PDF #49-1642); Table S2: BET results of HC and HC@ZrO₂-1; Table S3: The electrochemical properties of HC and HC@ZrO₂; Table S4: ICE literature comparison of improving HC anode of SIBs by surface engineering; Table S5: The fitted results of the EIS plots using the equivalent circuit in Figure S5b. References [22–24,27,47] are cited in the supplementary materials.

Author Contributions: Conceptualization, Y.L., C.W., and Y.B.; methodology, Y.G. and C.Y.; validation, Y.G. and C.Y.; formal analysis, Y.G.; investigation, Y.G.; resources, Y.L., C.W., and Y.B.; data curation, C.Y.; writing—original draft preparation, Y.G.; writing—review and editing, Y.L., J.Q., and Y.B.; visualization, Y.G.; supervision, Y.L., C.W., and Y.B.; project administration, Y.L.; funding acquisition, Y.L. and Y.B. All authors have read and agreed to the published version of the manuscript.

Funding: This work was supported by the National Natural Science Foundation of China (Grant Nos. 21975026, 22005033) and the Beijing Institute of Technology Research Fund Program for Young Scholars (No. XSQD-202108005).

Institutional Review Board Statement: Not applicable.

Informed Consent Statement: Not applicable.

Data Availability Statement: The data presented in this study are available on request from the corresponding author. The data are not publicly available due to confidentiality.

Acknowledgments: The authors would like to thank the National Natural Science Foundation of China (Grant Nos. 21975026, 22005033), and the Beijing Institute of Technology Research Fund Program for Young Scholars (No. XSQD-202108005) for the financial support of this project.

Conflicts of Interest: The authors declare no conflict of interest.

References

1. Dunn, B.; Kamath, H.; Tarascon, J. Electrical energy storage for the grid: A battery of choices. *Science* **2011**, *334*, 928–935. [[CrossRef](#)]
2. Yang, Z.; Zhang, J.; Kintner-Meyer, M.C.; Lu, X.; Choi, D.; Lemmon, J.P.; Liu, J. Electrochemical energy storage for green grid. *Chem. Rev.* **2011**, *111*, 3577–3613. [[CrossRef](#)]
3. Li, Y.; Qian, J.; Zhang, M.; Wang, S.; Wang, Z.; Li, M.; Bai, Y.; An, Q.; Xu, H.; Wu, F.; et al. Co-construction of sulfur vacancies and heterojunctions in tungsten disulfide to induce fast electronic/ionic diffusion kinetics for sodium-ion batteries. *Adv. Mater.* **2020**, *32*, 2005802. [[CrossRef](#)]
4. Yabuuchi, N.; Kubota, K.; Dahbi, M.; Komaba, S. Research development on sodium-ion batteries. *Chem. Rev.* **2014**, *114*, 11636–11682. [[CrossRef](#)]
5. Zhang, Q.; Lu, Y.; Guo, W.; Shao, Y.; Liu, L.; Lu, J.; Hu, Y. Hunting sodium dendrites in NASICON-based solid-state electrolytes. *Energy Mater. Adv.* **2021**, *2021*, 9870879. [[CrossRef](#)]
6. Hwang, J.; Myung, S.; Sun, Y. Sodium-ion batteries: Present and future. *Chem. Soc. Rev.* **2017**, *46*, 3529–3614. [[CrossRef](#)]
7. Vaalma, C.; Buchholz, D.; Weil, M.; Passerini, S. A cost and resource analysis of sodium-ion batteries. *Nat. Rev. Mater.* **2018**, *3*, 18013. [[CrossRef](#)]
8. Usiskin, R.; Lu, Y.; Popovic, J.; Law, M.; Balaya, P.; Hu, Y.; Maier, J. Fundamentals, status and promise of sodium-based batteries. *Nat. Rev. Mater.* **2021**, *6*, 1020–1035. [[CrossRef](#)]
9. Voronina, N.; Myung, S. Recent advances in electrode materials with anion redox chemistry for sodium-ion batteries. *Energy Mater. Adv.* **2021**, *2021*, 9819521. [[CrossRef](#)]

10. Sato, T.; Yoshikawa, K.; Zhao, W.; Kobayashi, T.; Rajendra, H.; Yonemura, M.; Yabuuchi, N. Efficient stabilization of Na storage reversibility by Ti integration into O'3-Type NaMnO₂. *Energy Mater. Adv.* **2021**, *2021*, 9857563.
11. Kubota, K.; Shimadzu, S.; Yabuuchi, N.; Tominaka, S.; Shiraiishi, S.; Abreu-Sepulveda, M.; Komaba, S. Structural analysis of sucrose-derived hard carbon and correlation with the electrochemical properties for lithium, sodium, and potassium insertion. *Chem. Mater.* **2020**, *32*, 2961–2977. [[CrossRef](#)]
12. Zhao, L.; Hu, Z.; Lai, W.; Tao, Y.; Peng, J.; Miao, Z.; Dou, S. Hard carbon anodes: Fundamental understanding and commercial perspectives for Na-ion batteries beyond Li-ion and K-ion counterparts. *Adv. Energy Mater.* **2020**, *11*, 2002704. [[CrossRef](#)]
13. Zhang, M.; Li, Y.; Wu, F.; Bai, Y.; Wu, C. Boost sodium-ion batteries to commercialization: Strategies to enhance initial Coulombic efficiency of hard carbon anode. *Nano Energy* **2021**, *82*, 105738. [[CrossRef](#)]
14. Dong, R.; Wu, F.; Bai, Y.; Li, Q.; Yu, X.; Li, Y.; Wu, C. Tailoring defects in hard carbon anode towards enhanced Na storage performance. *Energy Mater. Adv.* **2022**, *2022*, 9896218. [[CrossRef](#)]
15. Nita, C.; Zhang, B.; Dentzer, J.; Ghimbeu, C. Hard carbon derived from coconut shells, walnut shells, and corn silk biomass waste exhibiting high capacity for Na-ion batteries. *J. Energy Chem.* **2021**, *58*, 207–218. [[CrossRef](#)]
16. Hong, K.; Qie, L.; Zeng, R.; Yi, Z.; Zhang, W.; Wang, D.; Huang, Y. Biomass derived hard carbon used as a high performance anode material for sodium ion batteries. *J. Mater. Chem. A* **2014**, *2*, 12733–12738. [[CrossRef](#)]
17. Wang, C.; Su, W. Understanding acid pretreatment of lotus leaves to prepare hard carbons as anodes for sodium ion batteries. *Surf. Coat. Technol.* **2021**, *415*, 127125. [[CrossRef](#)]
18. Beda, A.; Escamilla-Pérez, A.; Simonin, L.; Matei Ghimbeu, C. Vegetal-extracted polyphenols as a natural hard carbon anode source for Na-ion batteries. *ACS Appl. Energy Mater.* **2022**, *5*, 4774–4787. [[CrossRef](#)]
19. Xiao, L.; Cao, Y.; Henderson, W.; Sushko, M.; Shao, Y.; Xiao, J.; Liu, J. Hard carbon nanoparticles as high-capacity, high-stability anodic materials for Na-ion batteries. *Nano Energy* **2016**, *19*, 279–288. [[CrossRef](#)]
20. Li, X.; Sun, X.; Hu, X.; Fan, F.; Cai, S.; Zheng, C.; Stucky, G. Review on comprehending and enhancing the initial Coulombic efficiency of anode materials in lithium-ion/sodium-ion batteries. *Nano Energy* **2020**, *77*, 105143. [[CrossRef](#)]
21. Lin, Q.; Zhang, J.; Lv, W.; Ma, J.; He, Y.; Kang, F.; Yang, Q. A functionalized carbon surface for high-performance sodium-ion storage. *Small* **2020**, *16*, 1902603. [[CrossRef](#)] [[PubMed](#)]
22. Xie, H.; Wu, Z.; Wang, Z.; Qin, N.; Li, Y.; Cao, Y.; Lu, Z. Solid electrolyte interface stabilization via surface oxygen species functionalization in hard carbon for superior performance sodium-ion batteries. *J. Mater. Chem. A* **2020**, *8*, 3606–3612. [[CrossRef](#)]
23. Yu, C.; Li, Y.; Ren, H.; Qian, J.; Wang, S.; Feng, X.; Liu, M.; Bai, Y.; Wu, C. Engineering homotype heterojunctions in hard carbon to induce stable solid electrolyte interfaces for sodium-ion batteries. *Carbon Energy* **2022**, 1–12. [[CrossRef](#)]
24. Li, Y.; Xu, S.; Wu, X.; Yu, J.; Wang, Y.; Hu, Y.; Huang, X. Amorphous monodispersed hard carbon micro-spherules derived from biomass as a high performance negative electrode material for sodium-ion batteries. *J. Mater. Chem. A* **2015**, *3*, 71–77. [[CrossRef](#)]
25. Ponrouch, A.; Palacín, M. On the high and low temperature performances of Na-ion battery materials: Hard carbon as a case study. *Electrochem. Commun.* **2015**, *54*, 51–54. [[CrossRef](#)]
26. He, X.; Zhao, J.; Lai, W.; Li, R.; Yang, Z.; Xu, C.; Wu, M. Soft-carbon-coated, free-standing, low-defect, hard-carbon anode to achieve a 94% initial Coulombic efficiency for sodium-ion batteries. *ACS Appl. Mater. Interfaces* **2021**, *13*, 44358–44368. [[CrossRef](#)]
27. Lu, H.; Chen, X.; Jia, Y.; Chen, H.; Wang, Y.; Ai, X.; Cao, Y. Engineering Al₂O₃ atomic layer deposition: Enhanced hard carbon-electrolyte interface towards practical sodium ion batteries. *Nano Energy* **2019**, *64*, 103903. [[CrossRef](#)]
28. Lin, Q.; Zhang, J.; Kong, D.; Cao, T.; Zhang, S.; Chen, X.; Yang, Q. Deactivating defects in graphenes with Al₂O₃ nanoclusters to produce long-life and high-rate sodium-ion batteries. *Adv. Energy Mater.* **2019**, *9*, 1803078. [[CrossRef](#)]
29. Feng, T.; Xu, Y.; Zhang, Z.; Du, X.; Sun, X.; Xiong, L.; Holze, R. Low-cost Al₂O₃ coating layer as a preformed SEI on natural graphite powder to improve Coulombic efficiency and high-rate cycling stability of lithium-ion batteries. *ACS Appl. Mater. Interfaces* **2016**, *8*, 6512–6519. [[CrossRef](#)]
30. Schipper, F.; Bouzaglio, H.; Dixit, M.; Erickson, E.; Weigel, T.; Talianker, M.; Aurbach, D. From surface ZrO₂ coating to bulk Zr doping by high temperature annealing of nickel-rich lithiated oxides and their enhanced electrochemical performance in lithium ion batteries. *Adv. Energy Mater.* **2018**, *8*, 1701682. [[CrossRef](#)]
31. Chen, Z.; Dahn, J. Effect of a ZrO₂ coating on the structure and electrochemistry of Li_xCoO₂ when cycled to 4.5 V. *Electrochem. Solid-State Lett.* **2002**, *5*, A213–A216. [[CrossRef](#)]
32. Yao, L.; Liang, F.; Jin, J.; Chowdari, B.; Yang, J.; Wen, Z. Improved electrochemical property of Ni-rich LiNi_{0.6}Co_{0.2}Mn_{0.2}O₂ cathode via in-situ ZrO₂ coating for high energy density lithium ion batteries. *Chem. Eng. J.* **2020**, *389*, 124403. [[CrossRef](#)]
33. Herzog, M.; Esken, D.; Janek, J. Improved cycling performance of high-nickel NMC by dry powder coating with nanostructured fumed Al₂O₃, TiO₂, and ZrO₂: A comparison. *Batteries Supercaps* **2021**, *4*, 1003–1017. [[CrossRef](#)]
34. Yano, A.; Ueda, A.; Shikano, M.; Sakaebe, H.; Ogumi, Z. Surface structure and high-voltage charging/discharging performance of low-content Zr-oxide-coated LiNi_{1/3}Co_{1/3}Mn_{1/3}O₂. *J. Electrochem. Soc.* **2015**, *163*, A75–A82. [[CrossRef](#)]
35. Laskar, M.; Jackson, D.; Xu, S.; Hamers, R.; Morgan, D.; Kuech, T. Atomic layer deposited MgO: A lower overpotential coating for Li[Ni_{0.5}Mn_{0.3}Co_{0.2}]O₂ Cathode. *ACS Appl. Mater. Interfaces* **2017**, *9*, 11231–11239. [[CrossRef](#)]
36. Zywootko, D.; Zandi, O.; Faguet, J.; Abel, P.; George, S. ZrO₂ Monolayer as a removable etch stop layer for thermal Al₂O₃ atomic layer etching using hydrogen fluoride and trimethylaluminum. *Chem. Mater.* **2020**, *32*, 10055–10065. [[CrossRef](#)]
37. Li, Y.; Yuan, Y.; Bai, Y.; Liu, Y.; Wang, Z.; Li, L.; Lu, J. Insights into the Na⁺ storage mechanism of phosphorus-functionalized hard carbon as ultrahigh capacity anodes. *Adv. Energy Mater.* **2018**, *8*, 170271. [[CrossRef](#)]

38. Komaba, S.; Murata, W.; Ishikawa, T.; Yabuuchi, N.; Ozeki, T.; Nakayama, T.; Fujiwara, K. Electrochemical Na insertion and solid electrolyte interphase for hard-carbon electrodes and application to Na-ion batteries. *Adv. Funct. Mater.* **2011**, *21*, 3859–3867. [[CrossRef](#)]
39. Dou, X.; Hasa, I.; Saurel, D.; Vaalma, C.; Wu, L.; Buchholz, D.; Passerini, S. Hard carbons for sodium-ion batteries: Structure, analysis, sustainability, and electrochemistry. *Mater. Today* **2019**, *23*, 87–104. [[CrossRef](#)]
40. Chen, F.; Di, Y.; Su, Q.; Xu, D.; Zhang, Y.; Zhou, S.; Pan, A. Vanadium-modified hard carbon spheres with sufficient pseudographitic domains as high-performance anode for sodium-ion batteries. *Carbon Energy* **2022**, 1–12. [[CrossRef](#)]
41. Yu, P.; Tang, W.; Wu, F.; Zhang, C.; Luo, H.; Liu, H.; Wang, Z. Recent progress in plant-derived hard carbon anode materials for sodium-ion batteries: A review. *Rare Met.* **2020**, *39*, 1019–1033. [[CrossRef](#)]
42. Wang, X.; Shi, J.; Mi, L.; Zhai, Y.; Zhang, J.; Feng, X.; Chen, W. Hierarchical porous hard carbon enables integral solid electrolyte interphase as robust anode for sodium-ion batteries. *Rare Met.* **2020**, *39*, 1053–1062. [[CrossRef](#)]
43. Qiu, S.; Xiao, L.; Sushko, M.; Han, K.; Shao, Y.; Yan, M.; Liu, J. Manipulating adsorption-insertion mechanisms in nanostructured carbon materials for high-efficiency sodium ion storage. *Adv. Energy Mater.* **2017**, *7*, 1700403. [[CrossRef](#)]
44. Sun, N.; Guan, Z.; Liu, Y.; Cao, Y.; Zhu, Q.; Liu, H.; Xu, B. Extended “adsorption-insertion” model: A new insight into the sodium storage mechanism of hard carbons. *Adv. Energy Mater.* **2019**, *9*, 1901351. [[CrossRef](#)]
45. Lu, H.; Ai, F.; Jia, Y.; Tang, C.; Zhang, X.; Huang, Y.; Cao, Y. Exploring sodium-ion storage mechanism in hard carbons with different microstructure prepared by ball-milling method. *Small* **2018**, *14*, 1802694. [[CrossRef](#)]
46. Ma, M.; Cai, H.; Xu, C.; Huang, R.; Wang, S.; Pan, H.; Hu, Y. Engineering solid electrolyte interface at nano-scale for high-performance hard carbon in sodium-ion batteries. *Adv. Funct. Mater.* **2021**, *31*, 2100278. [[CrossRef](#)]
47. Yu, C.; Li, Y.; Wang, Z.; Wang, X.; Bai, Y.; Wu, C. Surface engineering based on in situ electro-polymerization to boost the initial Coulombic efficiency of hard carbon anode for sodium-ion battery. *Rare Met.* **2022**, *41*, 1616–1625. [[CrossRef](#)]